Orbital Occupancy and Charge Doping in Iron-Based Superconductors

Claudia Cantoni, Jonathan E. Mitchell, Andrew F. May, Michael A. McGuire, Juan-Carlos Idrobo, Tom Berlijn, Elbio Dagotto, Matthew F. Chisholm, Wu Zhou, Stephen J. Pennycook, Athena S. Sefat, and Brian C. Sales*

Iron-based superconductors (FBS) comprise several families of compounds having the same atomic building blocks for superconductivity, but large discrepancies among their physical properties. A longstanding goal in the field has been to decipher the key underlying factors controlling the critical temperature for superconductivity (T_C) and the various doping mechanisms. In FBS materials this is complicated immensely by the different crystal and magnetic structures exhibited by the different families. In this paper, using aberration-corrected scanning transmission electron microscopy (STEM) coupled with electron energy loss spectroscopy (EELS), we observe a universal behavior in the hole concentration and magnetic moment across different families. All the parent materials have the same total number of electrons in the Fe 3*d* bands; however, the local Fe magnetic moment varies due to different orbital occupancy. Although the common understanding has been that both long-range and local magnetic moments decrease with doping, we find that, near the onset of superconductivity, the local magnetic moment increases and shows a dome-like maximum near optimal doping, where no ordered magnetic moment is present. In addition, we address a longstanding debate concerning how Co substitutions induces superconductivity in the 122 arsenide family, showing that the 3d band filling increases a function of doping. These new microscopic insights into the properties of FBS demonstrate the importance of spin fluctuations for the superconducting state, reveal changes in orbital occupancy among different families of FBS, and confirm charge doping as one of the mechanisms responsible for superconductivity in 122 arsenides. More generally, here we establish the validity of a method for comparing local magnetic moments that can be adopted for many other classes of Fe- and transition-metal-compounds, and used in the future to map the local magnetic moment with atomic spatial resolution. This will allow a deeper understanding of magnetic phenomena in technologically interesting materials.

Dr. C. Cantoni, J. E. Mitchell, Dr. A. F. May, Dr. M. A. McGuire, Dr. J.-C. Idrobo, Dr. M. F. Chisholm, Dr. W. Zhou, Dr. S. J. Pennycook, Dr. A. S. Sefat, Dr. B. C. Sales
Materials Science and Technology Division
Oak Ridge National Laboratory
Oak Ridge, TN 37831, USA
E-mail: cantonic@ornl.gov

Dr. J.-C. Idrobo, Dr. W. Zhou
Department of Physics and Astronomy
Vanderbilt University
Nashville, TN 37235, USA

Dr. J.-C. Idrobo, Dr. T. Berlijn
Center for Nanophase Materials Sciences
Oak Ridge National Laboratory
Oak Ridge, TN 37831, USA

Dr. T. Berlijn
Computer Science and Mathematics Division
Oak Ridge National Laboratory
Oak Ridge, Tennessee 37831, USA

Prof. E. Dagotto
Department of Physics and Astronomy
University of Tennessee
Knoxville, TN 37996, USA

DOI: 10.1002/adma.201401518

Extensive experimental and theoretical work has been carried out in recent years to gain a comprehensive understanding of the complex electronic structure of iron-based superconductors (FBS). Although a qualitative picture for pnictides has initially evolved based on common features, such as Fermi surface nesting between electron and hole pockets, and small magnetic moments in the paramagnetic state,[1–3] recent results for chalcogenides, i.e., $A_yFe_{2-x}Se_2$ (AFS) (A = alkali metal or alkaline-earth metal), have challenged those conclusions. The AFS have the largest magnetic moments among FBS and lack hole pockets in the Fermi surface.[4,5] Given the large differences in the electronic structure among FBS families, identifying the electronic features relevant for superconductivity has been a formidable challenge, making FBS particularly puzzling materials.

One of the most controversial aspects of FBS is their magnetism. Initially, the ordered magnetic state in FBS was described as a spin-density-wave related to the Fermi surface nesting and originating from itinerant electrons.[6] Currently, it is widely accepted that magnetic correlations in FBS cannot be solely explained by either a pure weak-coupling approach based on Fermi surface nesting, or a pure strong-coupling approach based on local moments.[7,8] AFS with composition $A_2Fe_4Se_5$ have the largest local magnetic moment (LMM), and for these materials, different experimental techniques as well as theoretical calculations agree on a magnitude of ca. 3.3 μ_B. For the other FBS, in particular pnictides, the situation is confusing. First-principles calculations, based on density functional theory (DFT) find the largest LMM with a magnitude of ca. 2 μ_B.[9,10] X-ray emission spectroscopy (XES)[11] and photoemission spectroscopy (PE)[12] find values ranging from 1.2 μ_B to 2.2 μ_B for 1111 (e.g., CeFeAsO) and 122 (e.g., $SrFe_2As_2$) parents, respectively, while conventional magnetic probes such as neutron scattering, Mössbauer, and muon spin rotation (μ-SR)[13] find the lowest values ranging from 0.9 μ_B for $BaFe_2As_2$ to ca. 0.3 μ_B for PrFeAsO. These discrepancies can be attributed to the rapid

temporal fluctuations of the local Fe moments, which enable only the techniques with the fastest response (PES, XES) to capture the instantaneous local moments, while conventional, slower techniques provide a time-averaged value. The situation is similarly confusing when describing the evolution of the LMM and electronic states with doping. There is no agreement among both theoretical and experimental studies on whether Co substitutions actually dope carriers in 122 arsenides. Although angle resolved photoemission spectroscopy (ARPES) experiments clearly show modifications of the Fermi surface consistent with charge doping,[14] X-ray absorption spectroscopy experiments reveal no change in the electronic occupation of Fe ions, and deduce that superconductivity is solely induced by bonding modifications.[15]

Some of the discrepancies found in the literature can be explained by realizing that FBS display different degrees of inhomogeneities, depending on details of growth methods and conditions. Inhomogeneities can include interstitials or vacancies forming either ordered or disordered clusters, strain, nanoscale variations in the dopant concentrations, and structural distortions, which have all been observed in FBS.

In this Letter, we report the local Fe magnetic moment across FBS families, free of the effects of extrinsic inhomogeneities, obtained in real space, with sub-nanometer resolution, and time-response as fast as electron dynamical processes (ca. 10^{-15} s), using EELS in the aberration-corrected STEM at room temperature. This extensive study involves data collected over four years on more than 50 TEM specimens.

We find that the local, room-temperature Fe magnetic moment varies significantly across the different families, reaching maximum values of ca. 3.3 μ_B in the AFS and minimum values of ca. 1 μ_B in the 1111 pnictides. Details of the Fe spectra indicate that the observed variations in LMM originate from different electron occupancies of the Fe 3*d* orbitals in different compounds. Surprisingly, the dependence of the local magnetic moment on doping is not monotonic as one would expect. A detailed analysis of the $Ba(Fe_{1-x}Co_x)_2As_2$ ($0 \le x \le 0.16$) system shows that the LMM drops significantly with increasing doping level at low Co concentrations, exhibiting a minimum close to the onset of superconductivity ($x \le 0.04$). However, for larger Co concentrations, the LMM increases showing a dome-like dependence with a maximum similar to T_C vs doping. Finally, we show direct evidence that the Fe 3*d* band filling increases as Co concentration increases in $Ba(Fe_{1-x}Co_x)_2As_2$, and therefore Co substitution for Fe does introduce carriers at the Fermi level in FBS.

Figure 1 is a collection of HAADF images from members of the 1111, 122, 11 (e.g., FeSe), and AFS families in different projections. These images show the exact regions from which the spectra were acquired (immediately before and/or after the images were taken) demonstrating the pristine conditions of the samples for which the magnetic moment was measured. The [100] projections (Figure 1a and 1d) clearly resolve the FeAs and FeSe layers common to all families, with the Fe columns appearing dimmer than the heavier As(Se) columns. In $TlFe_{1.6}Se_2$, ordered Fe vacancies arranged to yield a $\sqrt{5} \times \sqrt{5}$

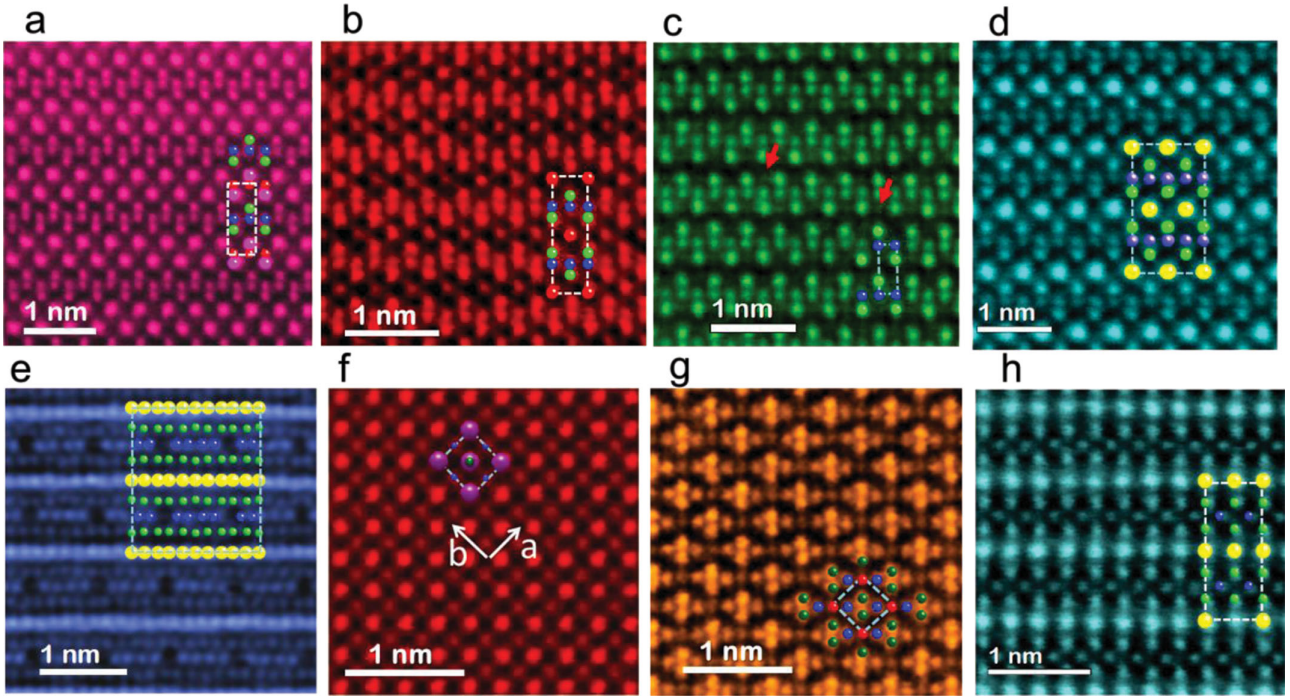

Figure 1. High-angle annular dark field (HAADF) STEM images of various FBS in different projections. a) PrFeAsO viewed along the [100] projection. Pr atoms are drawn in pink and O atoms are drawn in red. For all the drawings, the blue spheres indicate Fe atoms and the green spheres indicate As atoms. b) $Ca_{0.85}Pr_{0.15}Fe_2As_2$ ($T_C = 45$ K) [100] projection. Ca atoms are red. c) $Fe_{0.99}Te_{0.45}Se_{0.55}$ ($T_C = 14$ K) [100] projection. Te and Se atoms are green. The red arrows indicate interstitial Fe atoms. d) $TlFe_{1.6}Se_2$ having fully ordered Fe vacancies, [100] projection of the $ThCr_2Si_2$ subcell. Tl is yellow, Se green. e) $TlFe_{1.6}Se_2$ having fully ordered Fe vacancies, [110] zone-axis of the vacancy-ordered $\sqrt{5} \times \sqrt{5}$ supercell ([310] of the $ThCr_2Si_2$ subcell). Vacant Fe columns appear as dark spots. f) $BaFe_{1.92}Co_{0.08}As_2$ ($T_C = 24$ K), [001] projection. Ba is purple. g) $CaFe_2As_2$ [111] projection. h) $TlFe_{1.6}Se_2$ with disordered Fe [110] projection of the $ThCr_2Si_2$ cell.

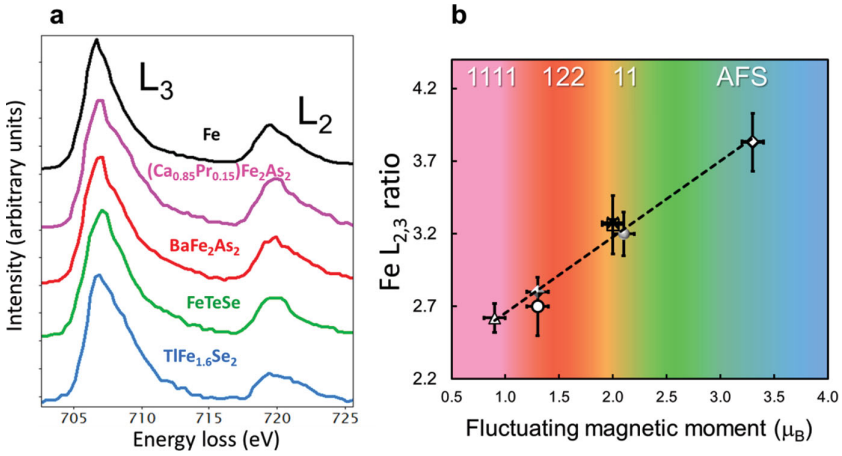

Figure 2. The Fe-$L_{2,3}$ ratio and its dependence on the local fluctuating Fe magnetic moment in FBS. a) comparison of Fe $L_{2,3}$ edges for Fe metal (black curve) and some of the compounds studied and plotted in (b). b) Plot of Fe $L_{2,3}$ ratio vs Fe LMM measured in refs. [10,11,25]. The plotted moment for FeSe and $Fe_{0.99}Te_{0.45}Se_{0.55}$ were taken both equal to $2\mu_B$ (the value reported in ref. [10] for $Fe_{1.2}Te$, $Fe_{1.03}Te$, and $FeTe_{0.3}Se_{0.7}$) because the whole series $FeTe_xSe_{1-x}$ $0 \le x \le 1$ is found to have similar LMMs (see ref. [25]). Data points were obtained by multiple measurements. From left to right: $(Ca_{0.85}Pr_{0.15})Fe_2As_2$ (Δ), CeFeAsO (○), $BaFe_2As_2$ (◒), FeSe (×), $Fe_{0.99}Te_{0.45}Se_{0.55}$ (□),$SrFe_2As_2$ (◒), and $TlFe_{1.6}Se_2$ (◇).

superstructure[16] are directly visible at specific projections, such as the [110] projection shown in Figure 1e.

Figure 2a shows the Fe-L edge acquired for metallic Fe, and different FBS and parent compounds. The local Fe magnetic moments were calculated by obtaining the ratio between the intensity of the L_3 and L_2 peaks (known as $L_{2,3}$ ratio) in the acquired Fe-L edge (see Supporting Information for details). L_3 and L_2 peaks arise from excitations of Fe $2p_{3/2}$ and $2p_{1/2}$ core electrons to unoccupied Fe 3*d* states, respectively. The detailed shape, position and intensity ratio of the L_3 and L_2 lines depends on several many-body effects and the ion's chemical environment. Specifically, the Fe $L_{2,3}$ ratio is sensitive to: i) the Fe oxidation state, ii) the Fe spin state, iii) the crystal field and local bonding.[17–19] Given the dependence on multiple parameters, the $L_{2,3}$ ratio is not typically used to estimate local magnetic moments in transition metal compounds. However, we show here that, in agreement with earlier studies of the $L_{2,3}$ ratio and LMM in Fe- and other transmission-metal-compounds by EELS and X-ray absorption spectroscopy,[20–24] in the case of FBS and their parents, Fe-$L_{2,3}$ spectra give a direct estimate of changes in the local Fe magnetic moment owing to the existence of a linear relationship between $L_{2,3}$ ratio and LMM.

Figure 2b shows a plot of the $L_{2,3}$ ratio for some of the compounds studied as a function of the local fluctuating Fe magnetic moment as reported in ref. [11,12,25] for the same compounds. The Fe $L_{2,3}$ ratio was measured for both [001] projections and [100] projections, and the two measurements gave almost identical values with the exception of the more anisotropic 1111 materials, for which the Fe $L_{2,3}$ ratios for the [100] projections were usually smaller than those for the [001] projection. Reported here are the average values of the measurements in both crystallographic directions. The spectra were collected averaging over regions of a few nm^2, and were insensitive to sample orientation and beam channeling, as it was experimentally verified (see the Supporting Information for more details).

The plot in Figure 2b indicates that the Fe $L_{2,3}$ ratio has a simple linear dependence on the Fe LMM in the high-temperature paramagnetic state. This empirical relationship finds a justification in the similar chemical and structural environment of the Fe ions in all the Fe-based compounds (characterized by analogous FeAs and FeSe(Te) planes with Fe in the same coordination and formal oxidation state), which leaves the spin state as the main variable affecting the Fe $L_{2,3}$ ratio, while crystal field and bonding effects produce negligible variations. This result is significant because it allows us to estimate Fe LMMs in FBS with sub-nanometer spatial resolution using EELS at room temperature (RT). We note from Figure 2b that the Fe $L_{2,3}$ ratio shows the smallest values for 1111 and 122 materials, intermediate values for the 11s and largest values for the AFSs, providing further experimental evidence of variation in LMM across the FBS families.

In addition to being a measure of the LMM, when summed and properly normalized, the integrated intensities of L_2 (I_{L2}) and L_3 (I_{L3}) provide an accurate estimate of the total number of holes in the 3*d* band.[26] Information about the distribution of the Fe 3*d* electrons is obtained considering the spin orbit interaction, which causes a small splitting of the final Fe 3*d* states with total angular momentum *j*, separating the total density of final states in partial densities relative to $j = 3/2$ and $j = 5/2$. Within the dipole approximation, one can derive an expression for the ratio of holes in $j = 5/2$ and $j = 3/2$ states given by:[21]

$$\frac{h_{5/2}}{h_{3/2}} = \frac{1}{6}\left[\frac{5I_{L_3}\omega_{L_2}}{2I_{L_2}\omega_{L_3}} - 1\right] \quad (1)$$

where ω_{L3} and ω_{L2} are the respective transition energies. By calculating the area under the Fe L_3 and the Fe L_2 peaks, it is thus possible to estimate the number of electrons in the Fe 3*d* band and obtain information about their distribution.

Figure 3a shows a plot of the ratio of holes in the $j = 5/2$ and $j = 3/2$ levels ($h_{5/2}/h_{3/2}$) and the total number of holes in the Fe 3*d* band as function of the Fe LMM for all the Fe-based families studied. The hole ratio follows the same trend as the Fe $L_{2,3}$ ratio across the families of Fe-based compounds with $(h_{5/2}/h_{3/2})1111 \le (h_{5/2}/h_{3/2})122 < (h_{5/2}/h_{3/2})11 < (h_{5/2}/h_{3/2})AFS$. However, the total number of holes does not correlate with the Fe LMM, being nearly constant in all the Fe-based compounds and equal to ca. 4. Figure 3a suggests that the difference in the Fe local magnetic moment among the different Fe-based compounds derives mainly from a varying distribution of the same number of electrons within the Fe 3*d* orbitals. The data are in agreement with recent theoretical calculations from Yin et al.,[27] which show that in going from the AFS to the 1111 in the order illustrated here, the distribution of electrons changes

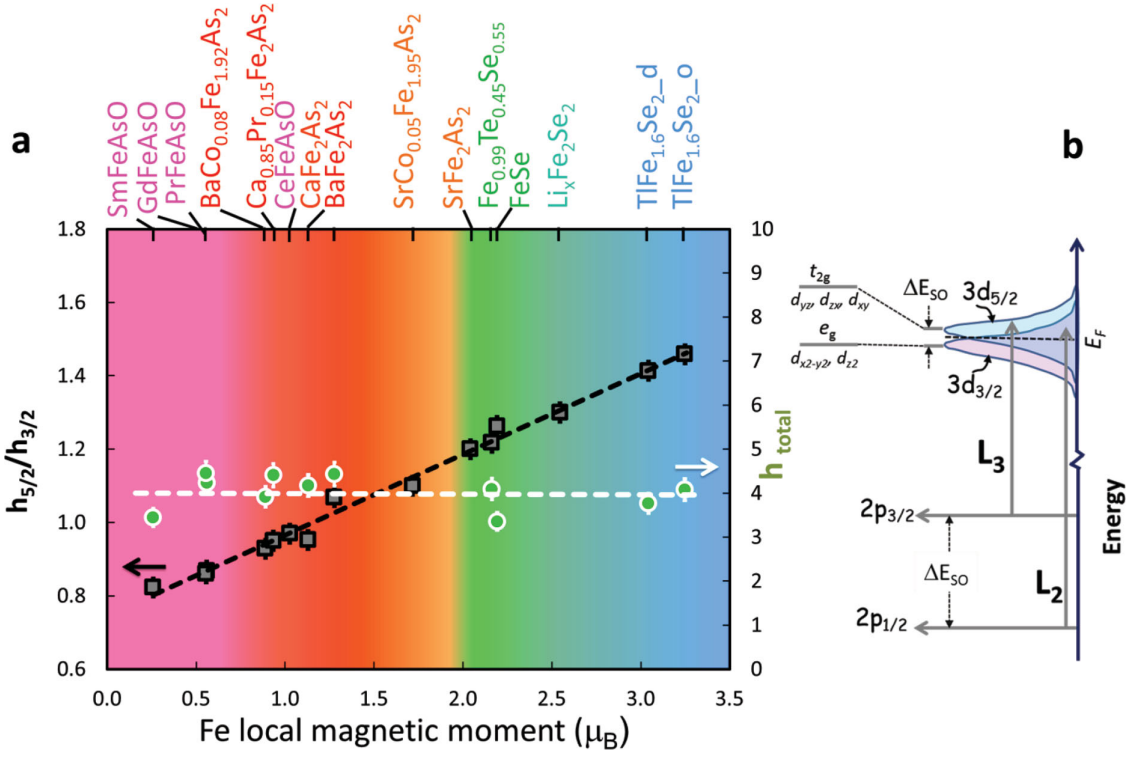

Figure 3. The ratio of holes in $j = 3/2$ and $j = 5/2$ (squares) and the total number of holes in the 3*d* band (circles) vs $L_{2,3}$ ratio. a) The ratio of holes increases according to the sequence $(h_{5/2}/h_{3/2})1111 \leq (h_{5/2}/h_{3/2})122 < (h_{5/2}/h_{3/2})11 < (h_{5/2}/h_{3/2})$AFS, indicating that different FBS families have different distributions of electrons in the Fe 3*d* orbitals. The total number of holes fluctuates around a value of ca. 4. Subscripts "o" and "d" for $TlFe_{1.6}Se_2$ refer to the compounds with ordered and disordered vacancies, respectively. b) Schematic of electronic transitions and atomic orbitals probed by the Fe-$L_{3,2}$.

as electron transfer occurs from the e_g to the t_{2g} orbitals, leaving the total Fe 3*d* occupancy unchanged.

As shown in the schematic of Figure 3b, the L_3 edge is generated by electronic transitions from filled $2p_{3/2}$ to empty $3d_{5/2}$ orbitals, while L_2 corresponds to transitions from filled $2p_{1/2}$ to empty $3d_{3/2}$ orbitals (dipole selection rules). Because the spin-orbit splitting is much larger for the 2*p* levels than the 3*d* levels, the L_3 always occurs at a lower energy than the L_2, independent on the actual distribution of the 3*d* orbitals, dictated by the combination of crystal field, electron correlations, and spin-orbit effects. The behavior of the hole ratio in Figure 3a indicates that the number of holes in the $3d_{5/2}$ orbitals increases with respect to the number of holes in the $3d_{3/2}$ orbitals in going from the 1111s to the AFSs. Therefore, the occupancy of the $3d_{5/2}$ orbitals progressively decreases from the 1111s to the AFSs but the total number of electrons in the 3*d* orbitals remains nearly constant. The explicit expressions of $3d_{3/2}$ and $3d_{5/2}$ orbitals in terms of t_{2g} (d_{yz}, d_{zx}, d_{xy}), and e_g ($d_{3z^2-r^2}$, $d_{x^2-y^2}$) orbitals can be calculated using the Clebsch–Gordan coefficients (as done in the Supporting Information) and the result shows that both $3d_{3/2}$ and $3d_{5/2}$ states are composed by 40% e_g states and 60% t_{2g} states. Therefore, the hole ratio we find cannot give direct information on the occupation of the specific orbitals; however, it can be used to test theoretical models of orbital occupation in different iron-based families. A calculation of the energy evolution of the $j = 5/2$ and $j = 3/2$ states from the limit of weak crystal field to that of strong crystal field for tetrahedral crystal fields (see Supporting Information) shows that $j = 5/2$ and $j = 3/2$ evolve separately into t_{2g} and e_g; as shown in the Energy scheme of Figure 3b.

A major concern in determining the relationships between LMM, band filling, and doping in Fe-based compounds is the ability to recognize and avoid the effects of structural and chemical inhomogeneities, which can only be done using spectroscopic techniques having nanoscale spatial resolution. In fact, STEM/EELS measurements show that the local Co concentration in $Ba(Fe_{1-x}Co_x)_2As_2$ crystals can change significantly on the nanometer scale depending on processing conditions. In addition, stacking faults are observed in cross section, which can also influence the measured electronic response (see Supporting Information). The simultaneous acquisition of high-resolution images and atomic-resolution EEL spectra in the STEM guarantees that contributions from defects, secondary phases and doping inhomogeneities can be excluded from the data. In order to explore the dependence of the Fe LMM on doping, images, spectra, and spectrum images were collected for a set of $Ba(Fe_{1-x}Co_x)_2As_2$ single crystals with x ranging from 0 to 0.16. The results are reported in **Figure 4**, as a plot of the Fe LMM as a function of the Co concentration derived by EELS using the same spectra from which the Fe $L_{2,3}$ ratio was calculated. The homogeneity of the Co concentration in the region from which the EEL spectra were acquired was determined by subsequently acquired spectrum images.

Figure 4 shows that the Fe LMM in the paramagnetic state rapidly decreases as compared to the moment of the parent compound for small Co additions in the range $0 < x \leq 0.04$.

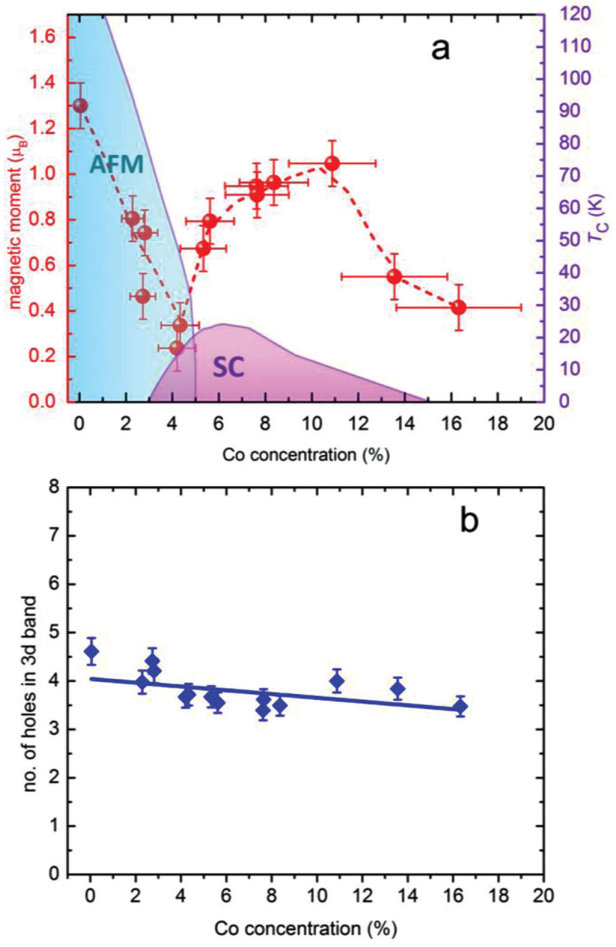

Figure 4. Local Fe magnetic moment and total number of holes in the Fe 3*d* orbitals in $Ba(Fe_{1-x}Co_x)_2As_2$ as function of local Co concentration. a) The EELS-derived Fe magnetic moment and overlaid $Ba(Fe_{1-x}Co_x)_2As_2$ phase diagram. Adapted with permission.[40] Copyright 2009, American Physical Society. b) The number of holes in the Fe 3*d* orbitals decreases as the Co concentration increases.

However, for Co concentrations above 4% ($T_C \approx 10$ K), the magnetic moment starts to increase, reaching a maximum near optimal doping, after which it decreases again as the Co concentration increases further. On the other hand, the total number of holes plotted in Figure 4b decreases, indicating a progressive filling of the Fe 3*d* bands with increasing Co concentration. Figure 4b is a clear indication that Co substitution contributes electrons to the Fe states above the Fermi level, which is in agreement with the notion of electron doping.

The LMM in optimally doped $Ba(Fe_{1-x}Co_x)_2As_2$ is about 30% smaller than in the parent compound. This difference is smaller than what found for $Sr(Fe_{1-x}Co_x)_2As_2$ in ref.[11] The reason could be related to doping inhomogeneity, which could yield a smaller LMM upon averaging, or might indicate that the maximum of the dome for $Sr(Fe_{1-x}Co_x)_2As_2$ is shifted towards higher Co concentrations. These finding are consistent with a recent study by resonant inelastic X-ray scattering, on optimally-doped superconducting $Ba_{0.6}K_{0.4}Fe_2As_2$, in which spin fluctuations as intense as in $BaFe_2As_2$ were measured.[28] Further agreement is found in ARPES,[13] resistivity,[28] Hall coefficient,[29,30] and thermoelectric power experiments, which show large Fermi surface modifications at small electron doping, just before the superconducting transition. As the Fermi surface reconstructs and the 3*d* orbitals shift with respect to the Fermi level as a function of doping, it is plausible that the dynamic Fe moment increases for $x > 0.04$ as a result to a transition to a higher spin state. Density of States calculations show[31] that in 122 arsenides the $d_{3z^2-r^2}$ orbital is nearly empty at the Fermi level, while the $d_{x^2-y^2}$ is mostly occupied. The other three d_{xy}, d_{yz}, d_{zx} show intermediate occupancy. Based on these calculations, we can focus our attention only on the $d_{3z^2-r^2}$, d_{xy}, d_{yz}, and d_{zx}, assuming that $d_{x^2-y^2}$ is full. We consider three of the orbitals (e.g., d_{xy}, d_{yz}, d_{zx}) as nearly degenerate and the other one ($d_{3z^2-r^2}$) to have a slightly higher energy. A possible explanation for the increase in LMM would be that a tendency to pair develops in the upper energy orbital. As a consequence, it may become energetically advantageous for the occupancy of this orbital to increase, giving rise to a higher spin state (see Supporting Information for a schematic model). Although there is evidence that superconductivity might not necessarily be driven by Fermi surface nesting, this tentative explanation certainly needs a more robust support from more sophisticated many-body calculations, which are beyond the scope of this paper. This "unoccupied" orbital may also be a band of states physically located somewhere else such as at the As atoms, that develops with doping. In fact, Co doping has shown to induce a change in the Fe-As bond distances,[32] which has been directly correlated to a change in local Fe magnetic moment.[33]

In conclusion, both the Fe local magnetic moment and Fe orbital occupations of FBS materials can be readily unveiled through the real space capability of aberration-corrected STEM. Bulk probes may miss subtle structural variations, making interpretation difficult or impossible. We have found that Fe 3*d* orbital occupancy is the key factor controlling the local Fe magnetic moment. In addition, although the ordering of Fe moments needs to be suppressed for superconductivity to arise, the local, fluctuating Fe magnetic moment is a key ingredient for the appearance of superconductivity. These are important steps towards an improved microscopic description of the appearance of superconductivity in Fe-based compounds.

Experimental Section

Simultaneous spectroscopy and high angle annular dark field (HAADF) imaging was conducted on nearly 50 samples at room temperature. The 11 chalcogenide, 122 arsenides, and AFS (with the exception of $Li_{0.5}Fe_2Se_2$) were single crystals grown out of self-flux.[34,35] 1111 samples are polycrystalline and were synthesized using a solid-state reaction.[36] Polycrystalline $Li_{0.5}Fe_2Se_2$ samples were produced by a liquid ammonia solvothermal technique.[37]

All single crystal samples were cleaved or cut and polished to about 20 µm in thickness using a precision polishing machine, and subsequently thinned to electron transparency (ca. 20 nm) by Ar ion milling at a voltage ≤ 3 kV with a final cleaning step at 0.5 kV. The microscope used for this study was a Nion UltraSTEM 100 operating at 100 kV[38] equipped with a second generation 5th order probe aberration corrector, a cold field emission electron gun, and a Gatan Enfina EEL spectrometer. This microscope routinely achieves a spatial resolution of 0.8 Å and has a maximum energy resolution of 300 meV. In some cases,

a Nion UltraSTEM 200 microscope operating at 200 kV,[39] was used, which is capable of higher spatial resolution as compared to the 100 kV electron microscope.

Supporting Information

Supporting Information is available from the Wiley Online Library or from the author.

Acknowledgements

Research was supported by the Materials Sciences and Engineering Division Office of Basic Energy Sciences, U.S. Department of Energy, and through a user project supported by ORNL's Center for Nanophase Materials Sciences (CNMS), which is sponsored by the Scientific User Facilities Division, Office of Basic Energy Sciences, U.S. Department of Energy. J.-C.I. and W.Z. acknowledge support from NSF grant No. DMR-0938330. T.B. was supported as a Wigner Fellow at the Oak Ridge National Laboratory.
Note: The author byline, the affiliations, the acknowledgements, and the caption to Figure 2 were corrected on September 11, 2014.

Received: April 3, 2014
Revised: June 5, 2014
Published online: July 28, 2014

[1] K. Kuroki, H. Usui, S. Onari, R. Arita, H. Aoki, *Phys. Rev. B* **2009**, *79*, 224511.
[2] K. Terashima, Y. Sekiba, J. H. Bowen, K. Nakayama, T. Kawahara, T. Sato, P. Richard, Y.-M. Xu, L. J. Li, G. H. Cao, Z.-A. Xu, H. Ding, T. Takahashi, *Proc. Natl. Acad. Sci. USA* **2009**, *106*, 7330.
[3] R. Thomale, C. Platt, W. Hanke, B. A. Bernevig, arXiv:1002.3599.
[4] Y. Zhang, L. X. Yang, M. Xu, Z. R. Ye, F. Chen, C. He, H. C. Xu, J. Jiang, B. P. Xie, J. J. Ying, X. F. Wang, X. H. Chen, J. P. Hu, M. Matsunami, S. Kimura, D. L. Feng, *Nat. Mater.* **2011**, *10*, 273.
[5] E. Dagotto, *Rev. Mod. Phys.* **2013**, *85*, 849.
[6] D. J. Singh, *Phys. Rev. B* **2008**, *78*, 094511.
[7] P. Dai, J. Hu, E. Dagotto, *Nat. Phys.* **2012**, *8*, 709.
[8] P. Hansmann, R. Arita, A. Toschi, S. Sakai, G. Sangiovanni, K. Held, *Phys. Rev. Lett.* **2010**, *104*, 197002.
[9] M. D. Johannes, I. I. Mazin, *Phys. Rev. B* **2009**, *79*, 220510.
[10] D. C. Johnston, *Adv. Phys.* **2010**, *59*, 803.
[11] H. Gretarsson, A. Lupascu, J. Kim, D. Casa, T. Gog, W. Wu, S. R. Julian, Z. J. Xu, J. S. Wen, G. D. Gu, R. H. Yuan, Z. G. Chen, N.-L. Wang, S. Khim, K. H. Kim, M. Ishikado, I. Jarrige, S. Shamoto, J.-H. Chu, I. R. Fisher, Young-June Kim, *Phys. Rev. B* **2011**, *84*, 100509(R).
[12] P. Vilmercati, A. Fedorov, F. Bondino, F. Offi, G. Panaccione, P. Lacovig, L. Simonelli, M. A. McGuire, A. S. Sefat, D. Mandrus, B. C. Sales, T. Egami1, W. Ku, N. Mannella, *Phys. Rev. B* **2012**, *85*, 220503(R).
[13] M. D. Lumsden, A. D. Christianson, *J. Phys. Condens. Matter* **2010**, *22*, 203203.
[14] C. Liu, T. Kondo, R. M. Fernandes, A. D. Palczewski, E. D. Mun, N. Ni, A. N. Thaler, A. Bostwick, E. Rotenberg, J. Schmalian, S. L. Bud'ko1, P. C. Canfield, A. Kaminski, *Nat. Phys.* **2010**, *6*, 419.
[15] M. Merz, F. Eilers, Th. Wolf, P. Nagel, H. v. Löhneysen, S. Schuppler, *Phys. Rev. B* **2012**, *86*, 104503.
[16] A. F. May, M. A. McGuire, H. Cao, I. Sergeev, C. Cantoni, B. C. Chakoumakos, D. S. Parker, B. C. Sales, *Phys. Rev. Lett.* **2012**, *109*, 077003.
[17] B. D. Leapman, L. A. Grunes, *Phys. Rev. Lett.* **1980**, *45*, 397.
[18] B. T. Thole, G. van der Laan, *Phys. Rev. B* **1988**, *38*, 3158.
[19] F. M. F. de Groot, *J. Electron. Spectrosc. Relat. Phenom.* **1994**, *61*, 529.
[20] H. Ardhuin, K. Suenaga, M. J. Casanove, E. Snoeck, C. Colliex, H. Fischer, S. Andrieu, M. Piecuch, *Phys. Rev. B* **1998**, *58*, 14135.
[21] T. I. Morrison, M. B. Brodsky, N. J. Zaluzec. *Phys. Rev. B* **1985**, *32*, 3107.
[22] H. Ikeno, T. Mizoguchi, Y. Koyama, Z. Ogumi, Y. Uchimoto, I. Tanaka, *J. Phys. Chem. C* **2011**, *115*, 11871.
[23] T. I. Morrison, C. L. Foiles, D. M. Pease, N. J. Zaluzec, *Phys. Rev. B* **1987**, *36*, 3739.
[24] H. Kurata, N. Tanaka, *Microsc. Microanal. Microstruct.* **1991**, *2*, 183.
[25] L. Simonelli, N. L. Saini, Y. Mizuguchi, Y. Takano, T. Mizokawa, G. Baldi, G. Monaco, *J. Phys.: Condens. Matter* **2012**, *24*, 415501.
[26] D. H. Pearson, C. C. Ahn, B. Fultz, *Phys. Rev. B* **1993**, *47*, 8471.
[27] Z. P. Yin, K. Haule, G. Kotliar, *Nat. Mater.* **2011**, *10*, 932.
[28] K.-J. Zhou, Y.-B. Huang, C. Monney, X. Dai, V. N. Strocov, N.-L. Wang, Z.-G. Chen, C. Zhang, P. Dai, L. Patthey, J. van den Brink, H. Ding, T. Schmitt, *Nat. Commun.* **2013**, *4*, 1470.
[29] F. Rullier-Albenque, D. Colson, A. Forget, H. Alloul, *Phys. Rev. Lett* **2009**, *103*, 057001.
[30] E. D. Mun, S. L. Bud'ko, N. Ni, A. N. Thaler, P. C. Canfield, *Phys. Rev. B* **2009**, *80*, 054517.
[31] D. Kasinathan, A. Ormeci, K. Koch, U. Burkhardt, W. Schnelle, A. Leithe-Jasper, H. Rosner, *New J. Phys.* **2009**, *11*, 025023.
[32] E. Granado, L. Mendonça-Ferreira, F. Garcia, G. De, M. Azevedo, G. Fabbris, E. M. Bittar, C. Adriano, T. M. Garitezi, P. F. S. Rosa, L. F. Bufaiçal, M. A. Avila, H. Terashita, P. G. Pagliuso, *Phys. Rev. B* **2011**, *83*, 184508.
[33] M. D. Johannes, I. I. Mazin, D. S. Parker, *Phys. Rev. B* **2010**, *82*, 024527.
[34] A. S. Sefat, R. Jin, M. A. McGuire, B. C. Sales, D. J. Singh, D. Mandrus, *Phys. Rev. Lett.* **2008**, *101*, 117004.
[35] B. C. Sales, A. S. Sefat, M. A. McGuire, R. Y. Jin, D. Mandrus, *Phys. Rev. B* **2009**, *79*, 094521.
[36] M. A. McGuire, A. D. Christianson, A. S. Sefat, B. C. Sales, M. D. Lumsden, R. Jin, E. A. Payzant, D. Mandrus, Y. Luan, V. Keppens, V. Varadarajan, J. W. Brill, R. Hermann, M. T. Sougarati, F. Grandjean, G. J. Lon, *Phys. Rev. B* **2008**, *78*, 094517.
[37] T. P. Ying, X. L. Chen, G. Wang, S. F. Jin, T. T. Zhou, X. F. Lai, H. Zhang, W. Y. Wang, *Sci. Rep.* **2012**, *2*, 426.
[38] O. L. Krivanek, G. J. Corbin, N. Dellby, B. F. Elston, R. J. Keyse, M. F. Murfitt, C. S. Own, Z. S. Szilagyi, J. W. Woodruff, *Ultramicroscopy* **2008**, *108*, 179.
[39] N. Dellby, N. J. Bacon, P. Hrncirik, M. F. Murfitt, G. S. Skone, Z. S. Szilagyi, O. L. Krivanek, *Eur. Phys. J.: Appl. Phys.* **2011**, *54*, 33505.
[40] C. Lester, J.-H. Chu, J. G. Analytis, S. C. Capelli, A. S. Erickson, C. L. Condron, M. F. Toney, I. R. Fisher, S. M. Hayden, *Phys. Rev. B* **2009**, *79*, 144523.